Effect of Eu^{2+} and Tb^{2+} doping on structural, photoluminescence, thermodynamic and thermoelectric properties of celestine (SrSO$_4$) phosphors

Abdul Ahad Khan [a], Zeesham Abbas [b], Zeshan Zada [c,*], Rifaqat Zada [d], Fazal Ur Rehman M [e], Muhammad Irfan [f], G. Murtaza [c,g], Muhammad Ismail [h], Qaisar Khan [i], Muhammad Ismail [j], Muhammad Ishaq [k], Sajjad Hussain [b], Ali H. Reshak [l,m,n]

[a] Department of Physics, University of Peshawar, Peshawar, 25120, Pakistan
[b] Department of Nanotechnology and Advanced Materials Engineering, Sejong University, Seoul, 05006, Republic of Korea
[c] Materials Modeling Lab, Department of Physics, Islamia College University, Peshawar, 25120, Pakistan
[d] Institute of Chemical Science, University of Peshawar, KPK, Pakistan
[e] Department of Chemistry, Lahore Garrison University, Pakistan
[f] Department of Physics, University of Sargodha, Sargodha, Punjab, Pakistan
[g] Department of Mathematics & Natural Sciences, Prince Mohammad Bin Fahd University, P. O. Box 1664, Alkhobar, 31952, Kingdom of Saudi Arabia
[h] School of Environment and Chemical Engineering, North China Electric Power University, Beijing, 102206, PR China
[i] Department of Physical and Biological Sciences, Islamia College Peshawar, Peshawar, 25120, Khyber Pakhtunkhwa, Pakistan
[j] Department of Chemistry, Women University Swabi, Swabi, KP, Pakistan
[k] Electrical Engineering Department, Comsats University Islamabad, Islamabad, 45550, Pakistan
[l] Physics Department, College of Science, University of Basrah, Basrah, 61004, Iraq
[m] Department of Instrumentation and Control Engineering, Faculty of Mechanical Engineering, Czech Technical University in Prague, Technicka 4, Prague 6, 166 07, Czech Republic
[n] Center of Excellence Geopolymer and Green Technology (CEGeoGTech), University Malaysia Perlis, 01007, Kangar, Perlis, Malaysia

HIGHLIGHTS

- Sr$_{1-x}$Eu$_x$SO$_4$ band profiles show semiconducting nature while the Sr$_{1-x}$Tb$_x$SO$_4$ depicts full-metallic nature.
- According to a theoretical assessment of optical properties, the compounds show prominent response in UV.
- The positive values of Seebeck coefficient exhibit hole carrier's dominancy.
- Sr$_{1-x}$Eu$_x$SO$_4$ and Sr$_{1-x}$Tb$_x$SO$_4$ compounds are promising for future advanced optical and thermoelectric devices.

ARTICLE INFO

ABSTRACT

In this study, the density functional theory (DFT) based WIEN2K simulation code is used to calculate the ground state properties of [SrSO$_4$]:Eu^{2+} and [SrSO$_4$]:Tb^{2+} compounds with the help of FP-LAPW method. To determine the electrical and optical characteristics of Sr$_{1-x}$A$_x$SO$_4$ (A = Eu^{2+}, Tb^{2+}), the Generalized gradient approximation with the addition of the Hubbard parameter (GGA + U) was utilized. The obtained band structure results of Sr$_{1-x}$Eu$_x$SO$_4$ compound show semiconducting nature (which is in the spin up (↑) state is 1.4eV while in the spin down (↓) state is 3.45eV), while the Sr$_{1-x}$Tb$_x$SO$_4$ compound depicts full-metallic nature through both spin states due to the crossing mechanisms of the conduction band minimum across the Fermi energy level. According to a theoretical assessment of optical properties, the compounds under investigation are promising possibilities for active optical devices working in the Ultra violet region. We have demonstrated in this work the variation of temperature (0–500 K) and pressure (0–10 GPa) on seven key thermodynamic parameters by Using quasi harmonic Debye model. The thermoelectric properties have been calculated in the temperature interval 500 K ≤ T ≤ 800 K by using the Boltzmann simulation code. The finding shows that Sr$_{1-x}$Eu$_x$SO$_4$ and Sr$_{1-x}$Tb$_x$SO$_4$ compounds are promising for future advanced optical and thermoelectric devices.

* Corresponding author.
E-mail address: zeshanzada@gmail.com (Z. Zada).

1. Introduction

Scientists always have interest in luminescence properties of novel storage materials having higher values of thermoluminescence (TL). With the improvement in nanotechnology, development of nano-phosphors with various designs is also a new trend because they are potential candidate to be used in technological applications like sensing, catalysis, photonics and electronics [1,2]. Nanostructured materials show remarkably improved properties (especially luminescence properties) as compared to the bulk material with same chemical formula [3]. Potential applications of these compounds have been found in radiation dosimetry as inspiringly established by the pioneering studies in this field [4]. Nanostructured phosphors may show different TL mechanism of energy transfer. Recombination of charge carriers and number of surface states increases by reducing the crystallites size of the materials that results in the enhancement of TL properties [5,6].

All branches of science dealing with ionizing radiations need an important instrument known as dosimeter [7]. The most appropriate tools to measure the absorbed dose are thermoluminescence dosimeters (TLDs). The process of light emission by an irradiated sample upon heating is known as thermoluminescence (TL). Properties of numerous TL materials had been investigated in nano, micro and bulk form to check their usability in dosimeters. Due to their potential applications in dosimeters, alkaline earth sulfates doped with rare earth (RE) elements are widely being studied by the researchers considering their radiation dose response range, low fading and detection of very small dose [8]. Researcher are trying to develop new alternatives of the phosphors [9–12]. Because of extremely high TL sensitivity, SrSO$_4$:Eu is a fascinating material [13]. But its long-term use in radiation measurements needed in environmental studies can sometimes be restricted by high fading. Zhang et al. [14], investigated the effect of Eu^{2+} and Eu^{3+} ions on TL properties of XSO$_4$ (X = Ca, Sr, Mg). They reported different emission temperatures and multiple emissions for both valence states of Eu. Q. Tang et al. [15], observed emission at 231 °C and reported that SrSO$_4$:Eu phosphors are highly sensitive to β-rays.

Further the non-classical process of fiber-by-fiber accumulation using poly (acrylic acid) in an aqueous solution system resulted in the biomimetic strain SrSO$_4$ crystals. In the early stage, crystals of polymer-stabilized fibrous hydrate 20–40 nm broad as well as several micrometers long were generated. The hydrous fibrils were then oriented attached to SrSO$_4$ microrods, which were subsequently dehydrated [16]. Repositories, radiation therapy rooms, and research facilities constructed using cement-based composites typically employed as an engineering barrier should be capable of handling exposure of radioactive applications. The Celestite (SrSO$_4$) minerals have been used as aggregates in barrier composites because of their high favorable performance both in mechanical and shielding capabilities of X-rays at certain levels [17]. In hydraulic fracturing systems, celestite (SrSO$_4$) precipitation is a frequent illustration of secondary sulphate mineral scaling problems, especially in basins with high quantities of strontium found naturally. In order to mitigate celestite along with other sulphate mineral scale under harsh circumstances typical of hydraulic fracturing in shale formations, future experimental research design may be guided by the findings of this research which lead to the formation of a new multicomponent reactive transport model [18].

From the above discussion, it is clear that there is still a lack of theoretical and experimental data on both these doped Sr$_{1-x}$A$_x$SO$_4$ (A = Eu^{2+}, Tb^{2+}) compounds. Several researchers have been reported first principle work [19–30] on other class of compounds like (Heusler, perovskite and Zintl compounds) for achieving their combine physical properties as we have discussed for the said doped compounds in the present work. The aim of this research was to look at the effect of doping Eu^{2+} and Tb^{2+} ions on photoluminescence, thermodynamic and thermoelectric properties of SrSO$_4$ by using first-principles DFT calculations. Deep understanding of the electronic properties of aforesaid compounds are obtained by calculating energy band structures and density of states (DOS). Usability of these compounds is checked by calculating optical parameters like refractive index, absorption coefficient, imaginary part of complex dielectric function and reflectivity etc. These results will be tremendously useful in conceptually understanding the photo-luminescence properties of aforementioned compounds theoretically. This article will provide a complete reference data to the experimentalists and theorists for further studies of these compounds.

2. Computational details

In this study, density functional theory (DFT) based WIEN2K simulation code is used to investigate ground state (optoelectronic & thermophysical) properties of [SrSO$_4$]:Eu^{2+} and [SrSO$_4$]:Tb^{2+} compounds with the assistance of FP-LAPW (full potential linearized augmented plane wave) method [31]. The optimized lattice parameters and structures are determined by using the PBE-GGA functional. Following that, the compounds' band structure, total and partial densities of states, and thermodynamic properties were all examined using relaxed geometry. In comparison to LDA/PBE-GGA, GGA + U is a thorough generalized approximation. Although LDA has been used to slowly fluctuating densities, it failed when the density changes quickly. In contrast to LDA, GGA provides superior findings in the domain of molecular geometries for the ground state energies, while d states are essentially unbound. This is because molecules hold the gradient of density at all coordinates. The Generalize Gradient Approximation (GGA) can be expressed as;

$$E_{xc}^{GGA}(n_\uparrow, n_\downarrow) = \int \varepsilon_{xc}(n_\uparrow, n_\downarrow, \nabla n_\uparrow, \nabla n_\downarrow) n(r) d^3 r \qquad (1)$$

Here, the electron charge densities for the spin up and down channels are represented by the numbers $n_\uparrow, n_\downarrow$, and the associated gradients are enhanced by the numbers $\nabla n_\uparrow, \nabla n_\downarrow$.

Generalized gradient approximation in addition to Hubbard parameter (GGA + U) [32] has been used to compute electronic and optical properties of Sr$_{1-x}$A$_x$SO$_4$ (A = Eu^{2+}, Tb^{2+}), where Hubbard parameter is the computational correction represented by U. The values of Hund's exchange (J) and Hubbard parameter (U) are 0 (screened exchange energy) and 7.1 eV, respectively. GGA + U model is often used with strongly correlated electron systems to get their improved ground states properties as noted by other work [33–35].

The main responsibility of U is to deal with on-site Coulomb interactions, which included localized electrons and a Hubbard-like terms defined the strongly correlated electrons system in which (d or f orbitals) are not filled. The strength of on-site interactions is determined by two parameters U and J, which are connected as U$_{eff}$ = U-J in ab-initio calculations. Hund's coupling is accounted by J, which is the exchange interaction term in the mentioned relation. For atoms with a partially filled d or f state, the value of U is set to 6.0 eV; in this study, Sr and Eu/Tb have a partially filled d state on which the GGA + U technique is implemented to account for self-interaction inaccuracy in d states [36, 37]. Wave functions were stretched up to a kinetic energy cutoff of 500 Ry, and energy convergence was set at 10^4. The DFT + U potential was utilized to calculate the optoelectronic properties of [SrSO$_4$]:Eu^{2+} and [SrSO$_4$]:Tb^{2+} compounds in order to study the onsite coulomb's interactions of Sr/Eu/Tb-d electrons.

For the material computations in the full potential scheme, the unit cell is divided into muffin tin and interstitial areas, the first of which is the product of a linear combination of wavefunctions and spherical harmonics, while the second of which is the expansion of the wave function into plane waves. In a full-potential system, the (core and valence) orbitals are treated by both relativistically and semi-relativistically methods. The unit cell's dimensions, shape, and relative atomic locations are relaxed to the point at which the force acting on each individual atom is less than 0.05 eV/Å. For Fourier expansions, the charge density G$_{max}$ = 12, (a$_0$)$^{-1}$ (where a$_0$ Bohr radius) is utilized. Brillouin zone (BZ) integrations are performed using a mesh of 1000 K-

points. The greatest value of the angular momentum function is set to 10 and the cut of energy RMT $k_{max} = 7$, where the first term indicates the lowest muffin tin radii and the second term represents the cut of the wave vector. The crystalline structures of [SrSO$_4$]:Eu^{+2} and [SrSO$_4$]: Tb^{+2} are shown in Fig. 1. Further the quasi-harmonic Debye model is used to investigate the thermodynamic findings [38–40]. The band structure results were employed in thermoelectric calculations through a Semi-classical Boltzmann transport theory [41].

3. Results and discussion

3.1. Electronic properties

3.1.1. Energy band structure

Energy band structures of Sr$_{1-x}$Eu$_x$SO$_4$ and Sr$_{1-x}$Tb$_x$SO$_4$ compounds for both spin up (↑) and spin down (↓) states are calculated along higher symmetry directions R-Γ-X-*M*-Γ of Brillouin zones (BZ) using GGA + U approximation and are shown in Fig. 2(a and b). The zero of the energy scales lies in between the valence and conduction band regions in both the compound band structures and is also named the Fermi energy level (E$_f$).

The maxima of Sr$_{1-x}$Eu$_x$SO$_4$ compound valence band and conduction band minima in both spin states are present at the Γ symmetric point, which means the nature of the energy bandgaps is direct with values in semiconductor range, which is in the spin up (↑) state is 1.4eV while in the spin down (↓) state is 3.45eV.

In the Sr$_{1-x}$Tb$_x$SO$_4$ compound, the prominent dispersion of a single conduction band is minimal at the high symmetry Γ point and also along Γ-M direction. Furthermore, the same band crosses the Fermi level and remains in the valence band region with absent overlapping in both spin orientations, clearly seen.

Overall, the Sr$_{1-x}$Eu$_x$SO$_4$ compound shows semiconducting nature through both spin states, while the Sr$_{1-x}$Tb$_x$SO$_4$ compound band structure depicts full-metallic nature due to the crossing mechanisms of the conduction band minimum across the Fermi energy level. Moreover, at the Femi level in both spin states, there is no energy gap that expresses the pure metallic nature of the Sr$_{1-x}$Tb$_x$SO$_4$ compound.

3.1.2. Density of states

The electronic properties of both these compounds Sr$_{1-x}$Eu$_x$SO$_4$ and Sr$_{1-x}$Tb$_x$SO$_4$ are the result of numerous possible electronic-transitions between conduction band (CB) and valence band (VB). The spectra of both total (TDOS) in Fig. 3 and partial (PDOS) density of states in Figs. 4 and 5 through both spin configurations can be used to examine the impact and contribution of various electronic states in the valence and conduction bands.

From Fig. 3 it is clear that over the entire energy range, both up and down spin (TDOS) have the exact similar variation (except at -2eV, a spike appears for Sr$_{1-x}$Eu$_x$SO$_4$ in the valence band region), which depicts that total magnetic moment in the whole energy range is zero for both the compounds.

From Fig. 4, we have noted that in the (VB) valence band the major contribution of oxygen (O-atoms) is in the energy range (-1.5eV to −4.3eV), while minor appearance of Eu and Sr-atoms are lie in the energy range (-1.8eV to -4eV) in both spin states. Whereas in the conduction band, the dominant contribution of *S*-atoms in the energy ranges (1.9eV–2.5eV and 3.6eV–5.5eV) and the minor appearance of Eu and Sr-atoms in the energy range (3.6eV–5.5eV) in both spin states are clearly observed from the compound PDOS spectra.

The major contributions in the lower energy valence band region are due to O[p] and Sr[p, d] orbitals, while minor Eu[d, f] and Sr[s] orbitals lie in both spin channels with the appearance of a minor peak of O[p] and major spike of Eu[f] at 0eV are also present. On the other hand, the major contributions in the lower and higher energy conduction band region are due to S[s], O and S[p], Eu and Sr[d] orbitals, respectively, while minor appearance of O[s], Eu[f] and Sr [s, p] orbitals lie in both spin channels.

From Fig. 5, we have noted that in the (VB) valence band the major contribution of oxygen (O-atoms) is in the energy range (-3.4eV to -6eV), while a spike of Tb-atoms at −4.5eV in the down spin state and a minor appearance of Sr-atoms are lie in the energy range (-4eV to -6eV) in both spin states. Whereas in the conduction band, dominant contribution of Tb-atoms in the energy ranges (1.4eV–4.5eV) and minor appearance of S and Sr-atoms in the energy range (1.6eV–3.5eV) and (3.6eV–6eV) respectively in both spin states are clearly observed from the compound PDOS spectra.

The major contribution in the lower energy valence band region is only due to O[p] orbitals lying in both spin channels, while a minor appearance of Tb[f] orbitals at further lower energy levels and a spike of the same Tb[f] orbital at 0eV is also present in the only down spin channel. On the other side, the major contributions in the lower and higher energy conduction band region are due to S[s], O and S[p], Tb and Sr[d] orbitals, respectively, while the minor appearance of O[s], Tb [f] and Sr [p] orbitals lie in both spin channels.

3.2. Optical properties

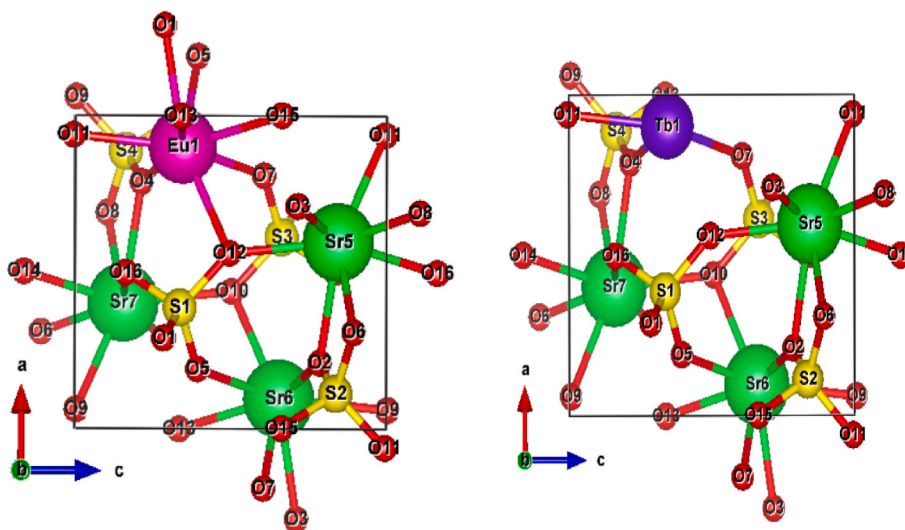The overall optical responses were plotted against the energy range

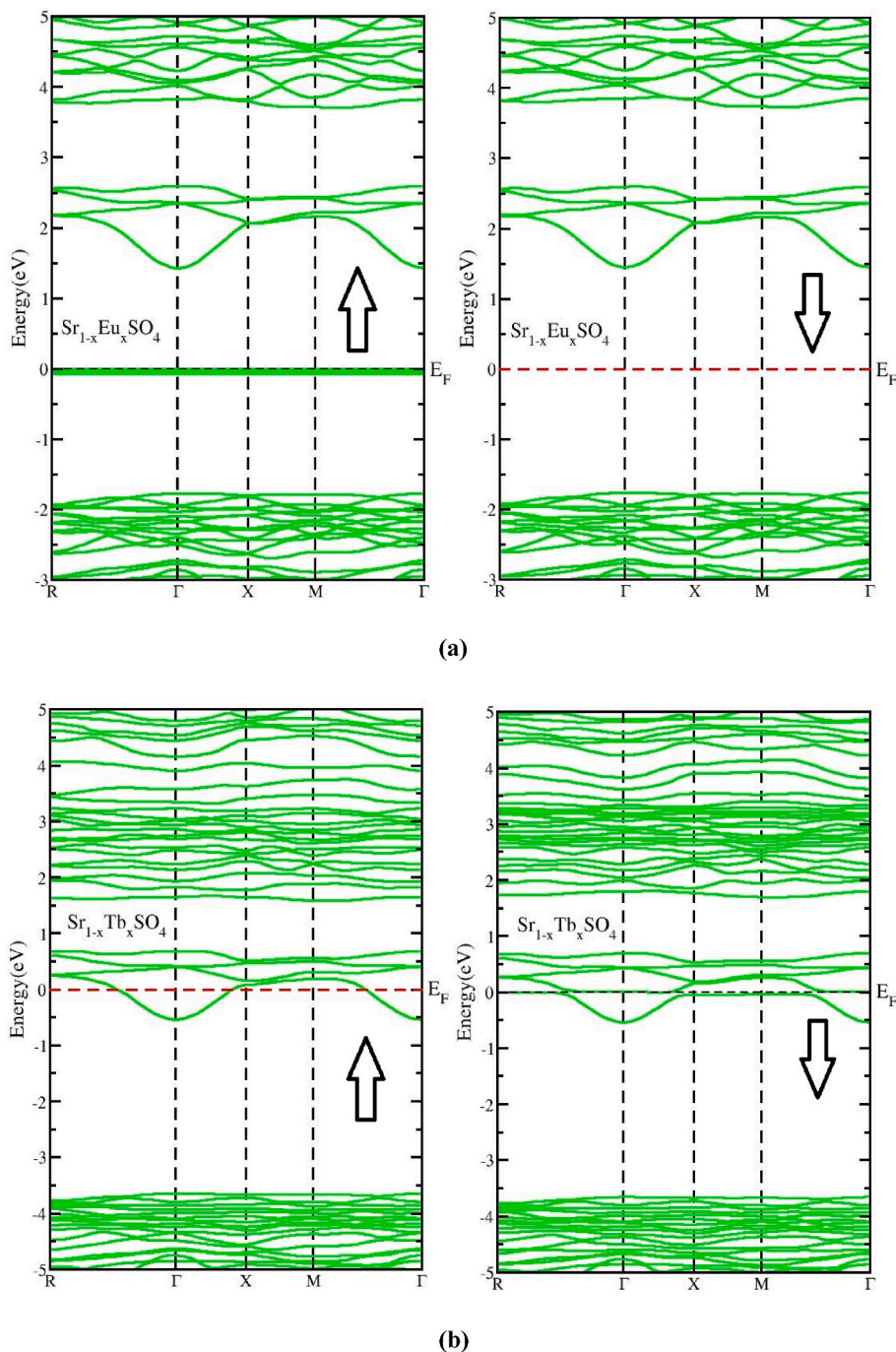**Fig. 1.** The Unit cell structures of [SrSO$_4$]:Eu^{+2} and [SrSO$_4$]:Tb^{+2}.

(a)

(b)

Fig. 2. Energy band structures of [SrSO$_4$]:Eu^{+2} and [SrSO$_4$]:Tb^{+2}.

in both spin orientations between 0 and 14eV as shown in Figures (4-9). The frequency (ω) dependent optical behavior of both the compounds Sr$_{1-x}$Eu$_x$SO$_4$ and Sr$_{1-x}$Tb$_x$SO$_4$ was investigated in terms of (linear optical response) theory.

The dielectric function $\varepsilon(\omega) = \varepsilon_1(\omega) + i\varepsilon_2(\omega)$, where $\varepsilon_1(\omega)$ is the real part (representing the material electronic polarizability) and $\varepsilon_2(\omega)$ is the imaginary part comprised of energy loss (material absorption capability), shows optical responses at all possible photon energies ($E = hc/\lambda$) of the material medium. The solid black lines represent (Eu doped Sr$_{1-x}$Eu$_x$SO$_4$) while the solid red lines represent the (Tb doped Sr$_{1-x}$Tb$_x$SO$_4$) in all the plotted optical parameters.

For Sr$_{1-x}$Eu$_x$SO$_4$ and Sr$_{1-x}$Eu$_x$SO$_4$ compounds, the real dielectric constant $\varepsilon_1(\omega)$ is a measure of the polarization of the material and the imaginary dielectric constant $\varepsilon_2(\omega)$ is a measure of the dielectric losses in

both spin orientations are plotted in Fig. 6.

The $\varepsilon_1(\omega)$ spectrum for Sr$_{1-x}$Eu$_x$SO$_4$ and Sr$_{1-x}$Tb$_x$SO$_4$ compounds start at low frequency in both spin orientations with values of 2.05 and 2.32 (spin up state) while 2 and -0.98 (spin down state) respectively, which is termed the static frequency limit of dielectric function.

It is clearly understood from the compounds energy band structure in Fig. 2, that there is a strong inverse relation between energy band gap of Sr$_{1-x}$Eu$_x$SO$_4$ (semiconductor) and the static $\varepsilon_1(0)$ dielectric constant followed by the known Penn model [42–44] as reported in other past studies in both spin orientations. While Sr$_{1-x}$Tb$_x$SO$_4$ (metallic) disobeys it due to the abrupt decline of the compound in the down spin state and the spectra $\varepsilon_1(\omega)$ obtaining the negative values (pure metallic character) in the low infrared region as well.

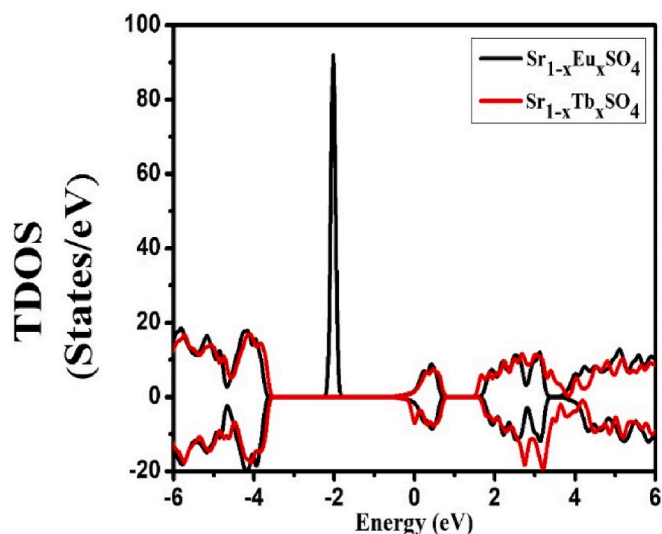Further beyond low frequency limits, $\varepsilon_1(\omega)$ gradually increases for

Fig. 3. Total density of states (TDOS) of [SrSO$_4$]: Eu^{+2} and [SrSO$_4$]: Tb^{+2}.

both compounds and reaches maximum obtained values of 2.89 at 5.537eV (spin up) and 2.88 at 5.537eV energy (spin down) for Sr$_{1-x}$Eu$_x$SO$_4$ while 3.3 at 5.455eV (spin up) and 3.19 at 5.510eV energy (spin down) for Sr$_{1-x}$Tb$_x$SO$_4$, respectively. Finally, we discovered that when the atoms Eu were replaced with Tb, the dominant peaks shifted to lower energies. The reported compounds main characteristic peaks are located in the visible high energy range, whereas some minor-peaks with shoulders lie in the low ultra-violet energy region of the electromagnetic spectrum.

After achieving maximum dominant peaks, the spectra of $\varepsilon_1(\omega)$ gradually decreases and reaches below zero (negative values) at specific energies of 11.877eV (spin up) and 11.904eV (spin down) for Sr$_{1-x}$Eu$_x$SO$_4$ while 11.687eV (spin up) and 11.687eV (spin down) for Sr$_{1-x}$Tb$_x$SO$_4$ compounds, respectively. Furthermore, the $\varepsilon_1(\omega)$ negative values in both spin orientations depict the overall attenuation of light in the optical medium for both the understudy compounds, the material

loses its complete dielectric property and displays metallic like character.

The plots of imaginary part $\varepsilon_2(\omega)$ for Sr$_{1-x}$Eu$_x$SO$_4$ and Sr$_{1-x}$Tb$_x$SO$_4$ through both spin orientations are shown in Fig. 6, which completely explains the possible absorptive behavior as well as the material band gaps. From the $\varepsilon_2(\omega)$ curves, the critical (starting point) occurs at about 1.646eV(spin up) and 4.068eV (spin down) closely related to the Sr$_{1-x}$Eu$_x$SO$_4$ compound band gap values, while the Tb based Sr$_{1-x}$Tb$_x$SO$_4$ compound shows absent critical values (no absorption) due to its metallic nature in both spin states.

The presence of these points is the attribution towards the electron optical transitions from the valence to the conduction band. As the electrons transition happens among different bands (inter-band transition), several major and minor peaks appear and are detected other than the threshold points. It can be further characterized by the electrons transition from O[p] and Sr[p, d] orbitals in the valence band to S[s], O/S[p] and Eu/Tb/Sr[d] orbitals in the conduction band for Sr$_{1-x}$Eu$_x$SO$_4$ and Sr$_{1-x}$Tb$_x$SO$_4$, respectively.

After getting the compounds threshold points, the curves increase almost gradually due to the enhancement of joint (density of states) in both spin orientations, contributing to imaginary part $\varepsilon_2(\omega)$. The dominant two peaks (with high values) in a spin up state with a shoulder appear, whereas major and minor peaks appearance (with high and low values) in spin down state is observed and noted in both these compounds.

However, the reported compounds maximum absorption capabilities with the main peaks of Sr$_{1-x}$Eu$_x$SO$_4$ have magnitudes of 2.39 at 9.293eV (spin up) and 2.35 at energy 9.319eV(spin down), while Sr$_{1-x}$Tb$_x$SO$_4$ has magnitudes of 2.35 at 9.347eV(spin up) and 2.42 at energy 9.319eV (spin down), respectively. Both the compounds main peaks lie in the high ultraviolet region whereas one moved towards higher in energy and became low (spin up) while the other remained at the same energy and became high (spin down) by replacing Eu by Tb. Furthermore, the dispersion spectrum of compounds covers up the whole ultraviolet energy region.

At the end, only Sr$_{1-x}$Eu$_x$SO$_4$ compound shows a band gap in both spin states, so being a medium band gap along with the dominant absorption in the both visible and ultraviolet (UV) energy ranges. Overall,
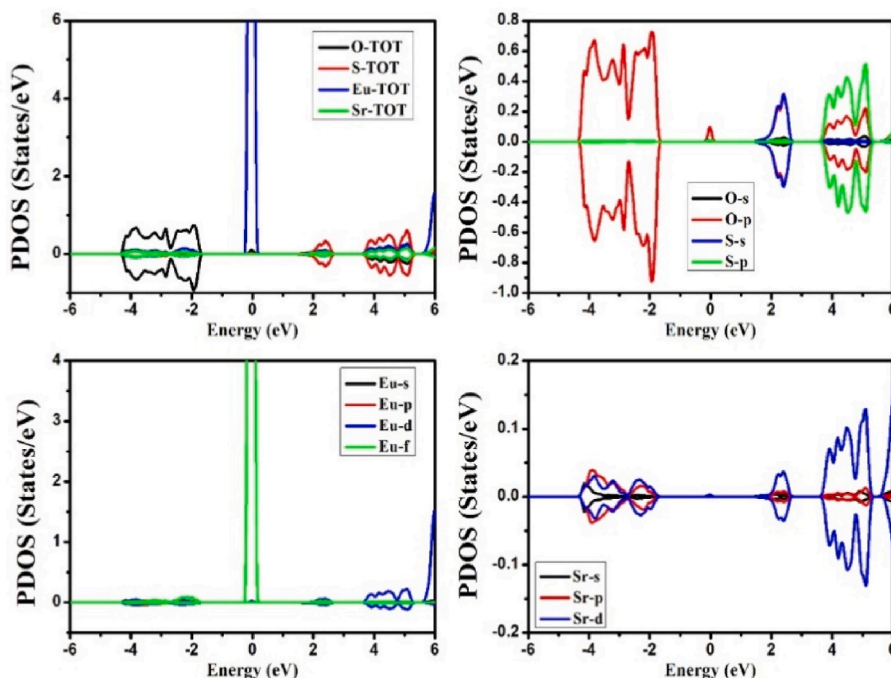

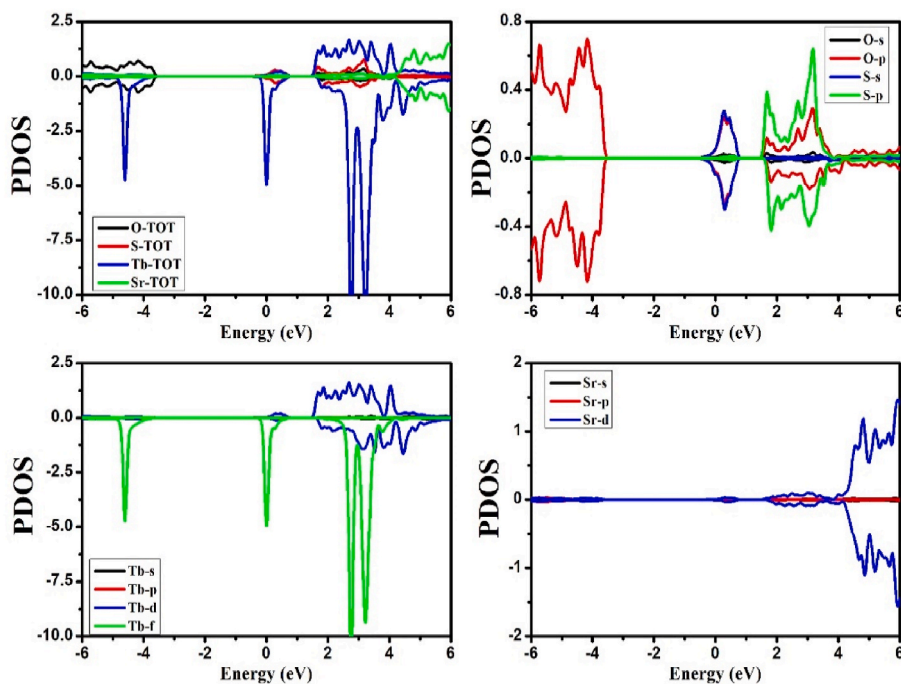**Fig. 4.** Partial density of states (PDOS) of [SrSO$_4$]:Eu^{+2}.

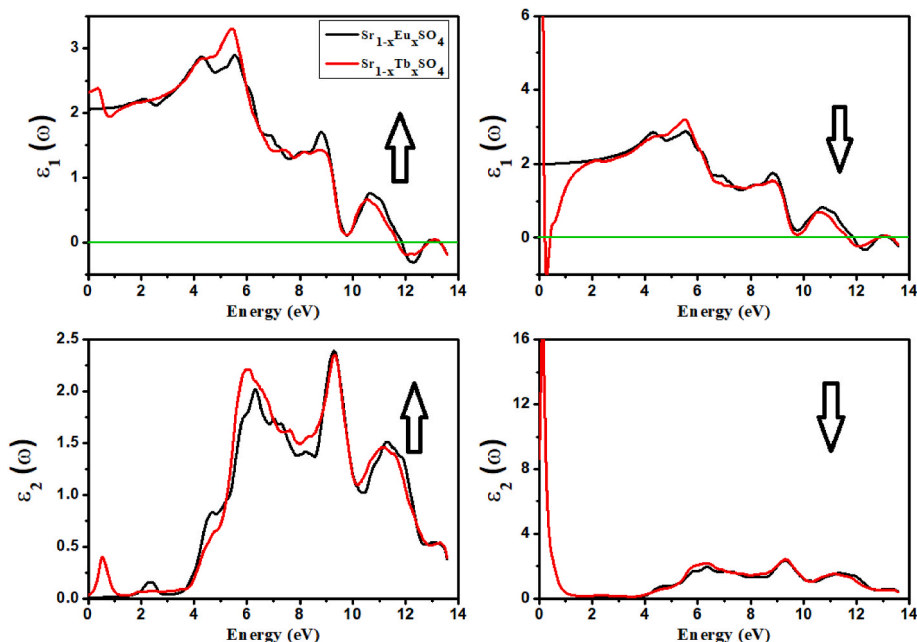**Fig. 5.** Partial density of states (PDOS) of $[SrSO_4]:Tb^{+2}$.

Fig. 6. Real $\varepsilon_1(\omega)$ and imaginary part $\varepsilon_2(\omega)$ of complex dielectric function of $[SrSO_4]:Eu^{+2}$ and $[SrSO_4]:Tb^{+2}$.

the material is claimed to be a good promising candidate for future solar-cell technology because it is stable and UV–Vis absorbent.

The refractive index $n(\omega)$ plays a key part in the consideration of material electronic properties. The plots of calculated refractive index $n(\omega)$ for $Sr_{1-x}Eu_xSO_4$ and $Sr_{1-x}Tb_xSO_4$ through both spin orientation are shown in Fig. 7.

Interestingly, $n(\omega)$ almost follows the similar behavior for both the compounds as $\varepsilon_1(\omega)$. The well-known theory [43,45–47] supports the similar trend of both $n(\omega)$ and $\varepsilon_1(\omega)$ spectra. The static $n(0)$ values of refractive indeces were found to be 1.43(spin up state) and 1.41(spin down state) for $Sr_{1-x}Eu_xSO_4$ while 1.52 (spin up state) and no such value of $n(0)$ for $Sr_{1-x}Tb_xSO_4$ were obtained due to the abrupt decline of the

compound spectra $n(\omega)$ in the (spin down state) in the low infrared region like $\varepsilon_1(\omega)$.

The maximum prominent peaks of $n(\omega)_{max}$ refractive index lie in the ultra-violet energy region with values of 1.74 (spin up state) and 1.73 (spin down state) appearing at the same energy of 5.646eV for $Sr_{1-x}Eu_xSO_4$ whereas 1.86 (spin up state) and 1.83 (spin down state) are noted at energies of 5.510eV and 5.565eV for $Sr_{1-x}Tb_xSO_4$ compound, respectively. It is clearly observed that the compounds with the smaller band gaps have higher refractive indeces. These reported results indicate that when the Eu is replaced by Tb, there is a decrease in $n(0)$ and $n(\omega)_{max}$, similar to $\varepsilon_1(0)$, while the opposite trend is present especially in the energy band gaps of the $Sr_{1-x}Eu_xSO_4$ compound.
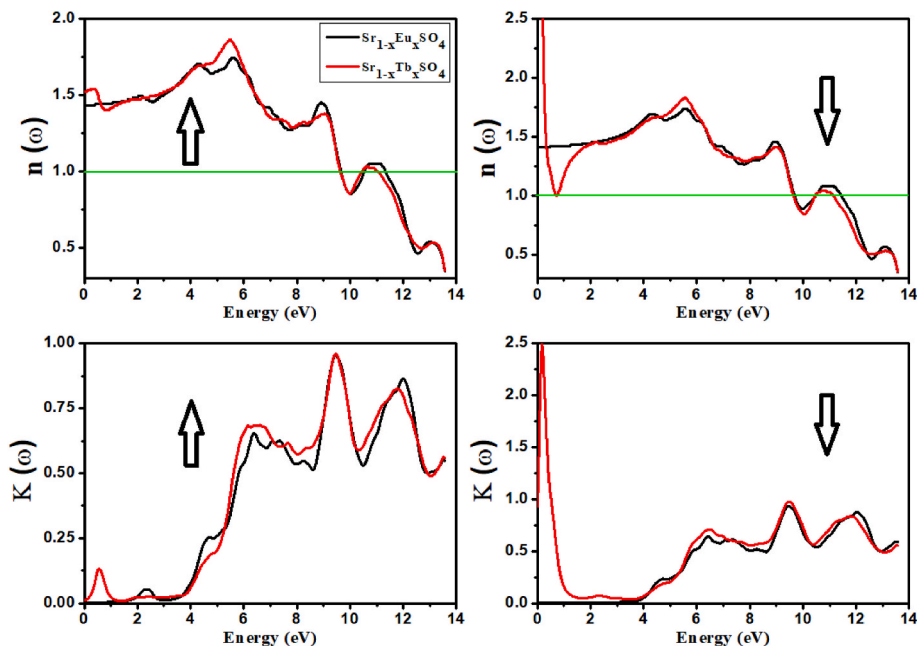
Fig. 7. Refractive index $n(\omega)$ and extinction coefficient $K(\omega)$ of [SrSO$_4$]:Eu^{+2} and [SrSO$_4$]:Tb^{+2}.

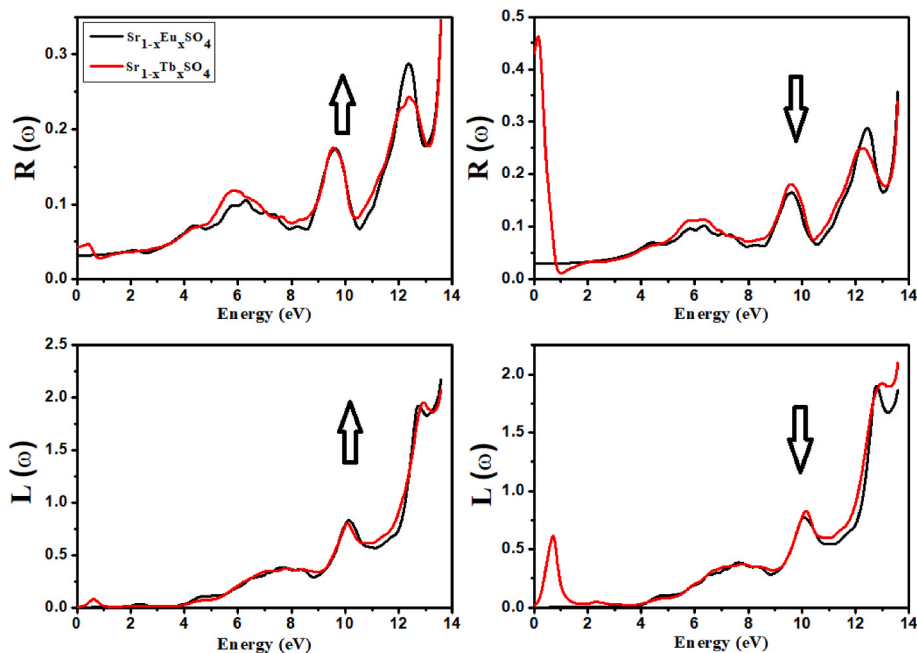**Fig. 8.** Reflectivity $R(\omega)$ and energy loss function $L(\omega)$ of [SrSO$_4$]:Eu^{+2} and [SrSO$_4$]:Tb^{+2}.

Overall, after achieving the maximum peak value the spectra decrease gradually (because the capabilities of material absorbing further incident light photon stops) with a few minor peaks appearing on the right side (high ultra-violet region) for both the compounds in both spin orientations.

These prominent decline in the peaks indicate dispersion with the photon energy. The refractive indices of both these compounds are high in the low-ultraviolet range, then gradually fall and remain in the high-ultraviolet energy range, as seen in the graphs.

The Extinction coefficients $K(\omega)$ declare a complete picture of the absorption capacity by passing the incident light through material. It relies on the incident photon energy as well as the material nature. The spectra of $K(\omega)$ through both spin orientations completely follow a similar pattern just like $\varepsilon_2(\omega)$ for Sr$_{1-x}$Eu$_x$SO$_4$ and Sr$_{1-x}$Tb$_x$SO$_4$ compounds as seen in Fig. 7.

From the $K(\omega)$ curves, the critical (starting point) occurs at about 1.809eV(spin up) and 3.905eV(spin down) closely related to the Sr$_{1-x}$Eu$_x$SO$_4$ compound band gap values, while the Tb-based Sr$_{1-x}$Tb$_x$SO$_4$ compound shows absent critical values (no absorption) due to its metallic nature in both spin states. After getting the compounds threshold points, the curves increase almost gradually in both spin orientations contributing to the imaginary part $\varepsilon_2(\omega)$. The dominant and major peaks (with high values) are observed and noted in both these compounds spin states.

However, the reported compounds maximum absorption capabilities $K(\omega)_{max}$ with the main peaks of Sr$_{1-x}$Eu$_x$SO$_4$ have magnitudes of 0.954

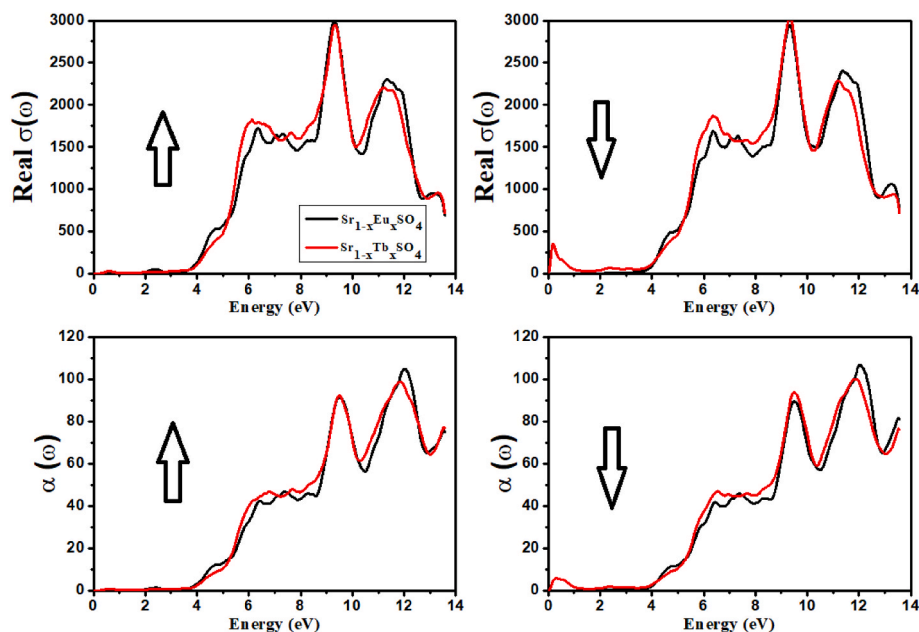**Fig. 9.** Real optical conductivity $\sigma(\omega)$ and absorption coefficient $\alpha(\omega)$ of $[SrSO_4]:Eu^{+2}$ and $[SrSO_4]:Tb^{+2}$.

(spin up) and 0.933(spin down) at energy of 9.455eV, while $Sr_{1-x}Tb_xSO_4$ has magnitude 0.96(spin up) and 0.978(spin down) at energy 9.483eV, respectively. Both the compounds main peaks lie in the high ultraviolet region whereas the spectra moved towards higher peak values by replacing Eu with Tb. Furthermore, the dispersion spectrum of compounds covers up the whole ultraviolet energy region.

Overall, $Sr_{1-x}Tb_xSO_4$ shows the maximum values in the ultraviolet region of extinction coefficient through both spin states which means (its ability to absorb light is much better in the UV region) as compared to the $Sr_{1-x}Eu_xSO_4$ compound.

The reflectivity $R(\omega)$, which is basically a frequency-dependent parameter through both spin orientations is plotted for $Sr_{1-x}Eu_xSO_4$ and $Sr_{1-x}Tb_xSO_4$ compounds in Fig. 8. The reflectivity spectrum for $Sr_{1-x}Eu_xSO_4$ and $Sr_{1-x}Tb_xSO_4$ compounds start at low frequency in both spin orientations with values of 3.17% and 4.31% (spin up state) while 2.94% and 43.1% (spin down state) respectively, which is termed as static frequency $R(0)$ limit of reflectivity. It is clearly understood, that there is a strong direct relation between static frequency $R(0)$ limit of $Sr_{1-x}Eu_xSO_4$ (semiconductor) and $Sr_{1-x}Tb_xSO_4$ (metallic) with the static $\varepsilon_1(0)$ dielectric constant in both spin orientations. Furthermore, it is obvious from the $R(\omega)$ spectra, the static value decreases for $Sr_{1-x}Eu_xSO_4$ due to the fact that the band gaps (spin up ($\uparrow$) state is 1.4eV while in spin down ($\downarrow$) state is 3.45eV) increased, which actually broadens the high-reflectivity range. While increases for $Sr_{1-x}Tb_xSO_4$ due to the (absent band gaps) metallic nature which further shortens the high-reflectivity range for the said compound.

Further beyond low frequency limits, $R(\omega)$ gradually increases with a few minor peaks for both compounds and reaches its maximum obtained values of 28.7% at 12.39eV (spin up) and 28.8% at 12.45eV energy (spin down) for $Sr_{1-x}Eu_xSO_4$ while 24.3% at 12.42eV (spin up) and 24.9% at 12.31eV energy (spin down) for $Sr_{1-x}Tb_xSO_4$, respectively. From these values, one can understand that maximum $R(\omega)$ reflection is depicted by the $Sr_{1-x}Eu_xSO_4$ compound in high energy range.

Finally, when the atoms Eu are replaced by Tb, the peaks shift toward higher energies (spin up) and lower energies (spin down) for both compounds. The reported compounds main characteristic peaks (maximum obtained values of $R(\omega)$) are located in the high ultra-violet energy range whereas some minor peaks with shoulders lie in low ultra-violet energy range of electromagnetic spectrum. By obtaining these results in the energy range between 4 and 14eV, the studied compounds

can be utilized as a shielding material due to high thermoelectric responses along with a promising blockage from solar heating in this region.

The energy loss function, $L(\omega)$, through both spin orientations is plotted for $Sr_{1-x}Eu_xSO_4$ and $Sr_{1-x}Tb_xSO_4$ compounds in Fig. 8. The said optical parameter tells us about the loss in energy of fast-moving electrons crossing the material that defines the Plasmon oscillations.

Initially the peak is absent (the spectral structure of $L(\omega)$ is approximately zero till 3.9 eV) for $Sr_{1-x}Eu_xSO_4$ while for $Sr_{1-x}Tb_xSO_4$ a minor peak appears in the infra-red region, and the points from where the peaks further begin to originate for compounds are also called threshold energy. There is a gradual increase in the spectra and resonant-peak that appears dominantly in the energy loss $L(\omega)$ spectrum is known as Plasmon peak.

The spectrum shows that Plasmon resonance with maximum peaks occurs at energies near 10eV and 12.0–14.0 eV through both spin orientations in the high UV region for both the compounds. The dominant peaks are assumed to appear due to the energy loss ($\varepsilon_1(\omega)$ approaches to zero at these lossless energy regions, as shown in our observations in Fig. 6.) of electrons, very likely caused by the electrons inelastic scattering within the materials.

The calculated optical conductivity $\sigma(\omega)$ spectra through both spin orientations is plotted for $Sr_{1-x}Eu_xSO_4$ and $Sr_{1-x}Tb_xSO_4$ compounds in Fig. 9. Initially there is no peak ($\sigma(\omega)$ is approximately zero till 3.9 eV (threshold energy)) noted for both the compounds through both spin orientations, and the points from where the peaks further begin to originate for compounds are also called threshold energy. There is a gradual increase in the conductivity spectra which further shows some prominent extreme values along with several minor peaks at particular-frequencies predict that optical conductivity occurs at different points over the entire high energy range for both compounds.

However, the extreme maximum values $\sigma(\omega)_{max}$ with the main peaks of $Sr_{1-x}Eu_xSO_4$ have magnitude of 2990 $\Omega^{-1}cm^{-1}$ at 9.32eV (spin up) and 2950 $\Omega^{-1}cm^{-1}$ at energy 9.35eV (spin down), while $Sr_{1-x}Tb_xSO_4$ has magnitude of 2950 $\Omega^{-1}cm^{-1}$ at 9.35eV (spin up) and 3000 $\Omega^{-1}cm^{-1}$ at energy 9.26eV (spin down), respectively. Beyond the maximum attaining values, the magnitude of ($\sigma(\omega)$ sharply decreases with the appearance of two minor peaks through both spin orientations in the high energy UV range.

Overall, it is interesting to note that the $Sr_{1-x}Tb_xSO_4$ shows the

maximum values in the ultraviolet region of $\sigma(\omega)$ through both spin states which means (the said material could be a potential candidate for the high-range frequency devices) as compared to $Sr_{1-x}Eu_xSO_4$ compound.

The calculated absorption coefficient $\alpha(\omega)$ spectra through both spin orientations is plotted for $Sr_{1-x}Eu_xSO_4$ and $Sr_{1-x}Tb_xSO_4$ compounds in Fig. 9. The said optical parameter tells us how far the incident photon with a specific energy in the material can penetrate before its complete absorption. Initially there is no peak ($\alpha(\omega)$ is approximately zero till 3.9 eV (threshold energy)) noted for both the compounds through both spin orientations, and the points from where the peaks further begin to originate for compounds are also called threshold energy.

There is a gradual increase in $\alpha(\omega)$ spectra beyond the threshold points for both the compounds and further show prominent extreme values along with two of the highest peaks in between 8 and 13eV, which indicate and proves that both these materials are the best absorber through both spin orientations and can be utilized as prospective candidates for the optical applications operated in high energy UV region.

However, the maximum $\alpha(\omega)_{max}$ values with the main peaks of $Sr_{1-x}Eu_xSO_4$ have magnitudes of $105 \times cm^{-1}$ (spin up) and $107 \times cm^{-1}$ (spin down) at the same energy 12.07eV, while $Sr_{1-x}Tb_xSO_4$ has magnitude of $98.9 \times cm^{-1}$ at 11.85eV (spin up) and $100 \times cm^{-1}$ at energy 11.93eV (spin down), respectively. Moreover, it is worth mentioning that the $Sr_{1-x}Eu_xSO_4$ shows the maximum value of $\alpha(\omega)$ as compared to the $Sr_{1-x}Tb_xSO_4$ compound, which means the absorption strength is decreasing by replacing Eu by Tb atom. Beyond the maximum attaining values, the magnitude of $\alpha(\omega)$ sharply decreasing through both spin orientations in the high energy UV range.

3.3. Thermodynamic properties

The exposure of material to high temperature and pressure ranges becomes very vital for complete understanding of material Thermodynamic side. We have demonstrated in this work the variation of temperature (0–500 K) and pressure (0–10 GPa) on seven key parameters like the unit cell volume variation (V), Entropy(S), Grüneisen parameter (γ), thermal expansion coefficient (α), specific heat at constant volume (C_v) along with constant pressure (C_P) and finally Debye temperature (θ_D).

The variation in unit cell volume (V) as a function of temperature at particular pressure ranges for $Sr_{1-x}Eu_xSO_4$ and $Sr_{1-x}Tb_xSO_4$ compounds have depicted in Fig. 10. A variation in V is quite similar and can be observed by changing pressure and temperature in the mentioned ranges for both the reported compounds. In all these curves by increasing pressure the decrease in volume occurs at a particular temperature while a lethargic increase in volume is found by increasing temperature at a particular pressure. Therefore, by enhancing temperature volume plus inter atomic distance increases whereas a dominant reverse trend with pressure for both compounds is obtained. The same behavior is frequently found in almost all solid materials because under temperature material expands while under pressure material compresses. Overall, the pressure effect is more dominant on the volume as compared to temperature.

Entropy (S), a thermodynamic parameter, deals with a system's disorder and also gives information on the system's real physical state. Fig. 11 depicts the fluctuation of the degree of order and disorder of $Sr_{1-x}Eu_xSO_4$ and $Sr_{1-x}Tb_xSO_4$ compounds with regard to pressure and temperature. Both the plots demonstrate that till 50 K entropy is zero at 0 GPa pressure, and it begins to increase further exponentially as temperature rises at the given pressure. The entropy value is rising which implies that the degree of disorder in both the compounds increases with increasing temperature. At 300 K and 0 GPa, the values are 396 J/mol K for $Sr_{1-x}Eu_xSO_4$ and 395 J/mol K for $Sr_{1-x}Tb_xSO_4$, according to our calculations. Such a rise in entropy is minimal at further higher temperatures, which is related to an increase in the vibrations of the atoms, and
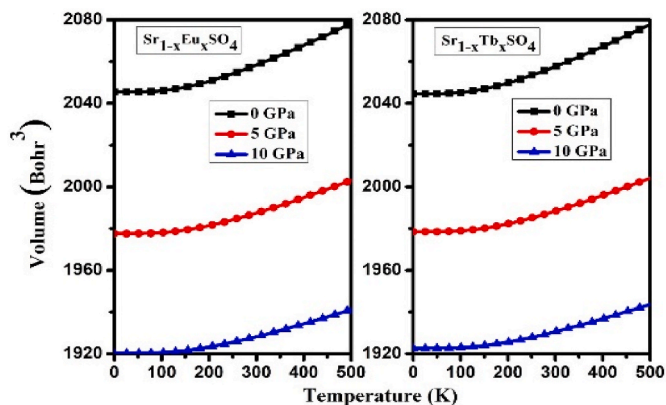

Fig. 10. Volume variation at various pressures and temperatures for [SrSO$_4$]: Eu^{+2} and [SrSO$_4$]:Tb^{+2}.

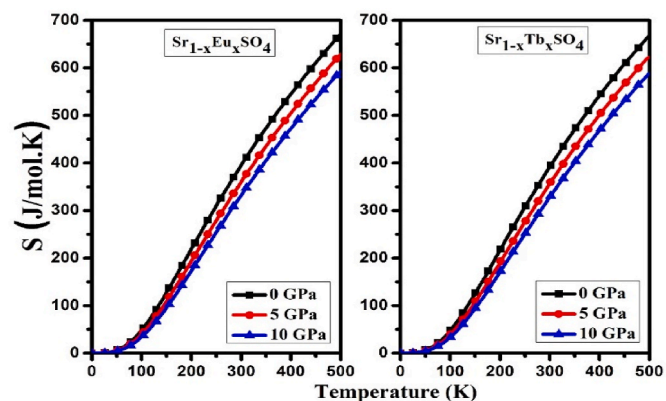**Fig. 11.** Calculated entropy at various pressures and temperatures for [SrSO$_4$]: Eu^{+2} and [SrSO$_4$]:Tb^{+2}.

thus the system's internal-energy rises.

Fig. 11 depicts the fluctuation of entropy as a function of pressure at a certain temperature. It has further been discovered that its magnitude reduces with increasing pressure at the specific temperature, indicating that with greater pressure the material becomes more ordered. Overall, the fluctuation in entropy with respect to temperature and pressure does not exhibit any inconsistency in the data, indicating the existence of a single phase.

The Gruneisen parameter (γ) is a crucial parameter for defining the softening and hardening of phonon modes in materials, especially when temperature and pressure are varied. Further it accurately predicts anharmonic characteristics of materials, such as thermal expansion coefficient and phonon frequency temperature dependency [48,49].

The influence of temperature and pressure on the Gruneisen parameter for $Sr_{1-x}Eu_xSO_4$ and $Sr_{1-x}Tb_xSO_4$ compounds is shown in Fig. 12. Both the plot shows that as temperature rises, γ decreases slowly and under various pressure levels, but as pressure rises with a step size of 5 GPa (from 0 to 10 GPa) at various temperature values, a quick reduction occurs in γ.

Overall, the influence of pressure on γ is greater than the effect of temperature. At 0 K and 0 GPa, we have reported values of 3.95×10^{-5} for $Sr_{1-x}Eu_xSO_4$ and 5.21×10^{-5} for $Sr_{1-x}Tb_xSO_4$, which drops to 6.19×10^{-6} for $Sr_{1-x}Eu_xSO_4$ and -5.85×10^{-6} for $Sr_{1-x}Tb_xSO_4$ at 0 K temperature and 10 GPa pressure, indicating that the lattice's anharmonicity is diminishing.

For solids, the thermal expansion coefficient (α) is responsible for tiny changes in dimension with temperature under constant pressure, as well as defining a parametric value for the measurements of bonding,
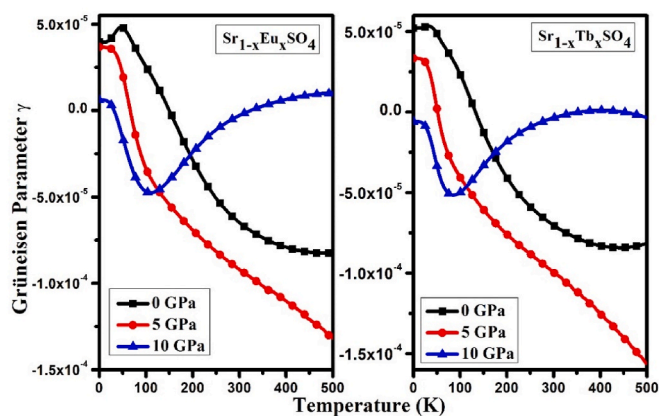
Fig. 12. Calculated Gruneisen parameter at various pressures and temperatures for [SrSO$_4$]:Eu^{+2} and [SrSO$_4$]:Tb^{+2}.

anharmonic effect and melting temperature. Temperature and pressure cause solids to expand and contract. As a result, we showed the thermal expansion coefficient of Sr$_{1-x}$Eu$_x$SO$_4$ and Sr$_{1-x}$Tb$_x$SO$_4$ compounds as a function of temperature and pressure in Fig. 13. Figure depicts that by increasing temperature, fast increase in α (expansion of the materials) occurs up to 300 K owing to the (Debye T^3 law) anharmonic effect, then α increases further slowly at a given pressure.

On the other hand, its value drops dramatically as pressure rises (solid compression) at a given temperature; these results are analogous to the C$_V$ variation. At the lower pressure step (0 GPa), the larger values of α are estimated and reported. Further the thermal expansion coefficient is also linked to the strength of atomic bonding and the melting temperature. In the solid, a higher α value indicates weak bonding while a smaller α value corresponds to strong bonding. Furthermore, strong bonding leads to solid with high melting point, whereas weak bonding correlates to a low melting point. As a result, we have attempted to offer first time a comprehensive analysis of Sr$_{1-x}$Eu$_x$SO$_4$ and Sr$_{1-x}$Tb$_x$SO$_4$ compounds thermal properties, which opens the door to additional future experimental investigation.

The knowledge and evolution of specific heat (C$_V$) at constant volume gives overall information about the nature of molecules motion, lattice vibration as well as phase transition. A clear decrease in C$_V$ curve is observed with a step size of 5 GPa(from 0 to 10Gpa) for both Sr$_{1-x}$Eu$_x$SO$_4$ and Sr$_{1-x}$Tb$_x$SO$_4$ compounds whereas a clear gradual increasing trend are noted over the entire temperature ranges as depicted in Fig. 14. The plots indicate that both temperature and pressure variation have almost similar notable impact with opposite trend on the compound C$_V$ values.
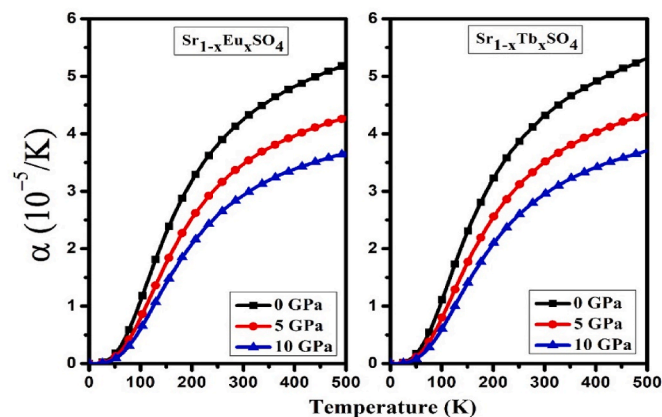
For a given pressure, the influence of temperature is more noticeable than the effect of pressure for a given temperature. C$_V$ correlates to the T^3 law at low temperatures (<300 K) owing to the anharmonic effect of the Debye model. Further at 0 Gpa and 300 K, the obtained value of specific heat is 477 Jmol^{-1}K^{-1} for Sr$_{1-x}$Eu$_x$SO$_4$ and Sr$_{1-x}$Tb$_x$SO$_4$ compounds. Finally rise in temperature (over θ$_D$) decreases anharmonicity and causes the C$_V$ to become practically constant for noted pressure ranges, indicating the Dulong-Petit limit [50–54]. This particular point denotes the excitation of phonon modes by thermal energy.

A clear decrease in specific heat (CP) curve is observed with a step size of 5Gpa (from 0 to 10Gpa) for both Sr$_{1-x}$Eu$_x$SO$_4$ and Sr$_{1-x}$Tb$_x$SO$_4$ compounds, whereas a clear gradual increasing trend is noted between 0 and 500 K temperature as depicted in Fig. 15. Moreover, we can see that when temperature rises, the variation in C$_P$ at lower and higher temperatures is comparable (similar trend) to C$_V$, but for both the compounds, C$_P$ appears to display similar characteristics under the mentioned pressures. C$_P$ declines as pressure increases (from 0 to 10 Gpa) and does not completely converge (beyond 130 K) at a constant value.

The Debye temperature (θ$_D$) is a crucial thermodynamic term in the quasi-harmonic Debye model to comprehending the vibrations in the lattice. When the temperature is below the Debye temperature, the vibrations in the material are caused by acoustic vibrations, but they have a minor influence when the temperature is above the Debye temperature. A clear increase in the θ$_D$ curve is observed with a step size of 5 GPa (from 0 to 10Gpa) for both Sr$_{1-x}$Eu$_x$SO$_4$ and Sr$_{1-x}$Tb$_x$SO$_4$ compounds, whereas clear gradual decreasing trends with a moderate pace are noted over the entire temperature ranges as depicted in Fig. 16. The plots indicate that both temperature and pressure variation have an almost similar notable impact, with the opposite trend on the compound θ$_D$ values. So, for Sr$_{1-x}$Eu$_x$SO$_4$ and Sr$_{1-x}$Tb$_x$SO$_4$ compounds, the reported values of θ$_D$ at 300 K (room temperature) and (0 GPa) of pressure are 656.88 K and 660.82 K, respectively.

A substance's bulk modulus is described as its resistance to compression and sensitivity to temperature and pressure. Temperature and pressure have an influence on materials, resulting in softness and strain, respectively. The fluctuation of bulk modulus with temperature at certain pressures from 0 to 10 GPa is shown in Fig. 17. At a given pressure, the bulk modulus falls as temperature rises. At 0 GPa and 0 K, it has a value of 138.36 GPa and 141.88 GPa, which drops to 125.41 GPa and 127.98 GPa at 0 GPa and 500 K for Sr$_{1-x}$Eu$_x$SO$_4$ and Sr$_{1-x}$Tb$_x$SO$_4$ compounds, respectively. At temperatures up to 500 K, the bulk modulus grows monotonously with increasing pressure at every step size of 5 GPa (from 0 to 10Gpa). The variation of the bulk modulus as temperature and pressure function is pretty general, with increasing temperature reducing hardness and increment in pressure causing stress in materials.
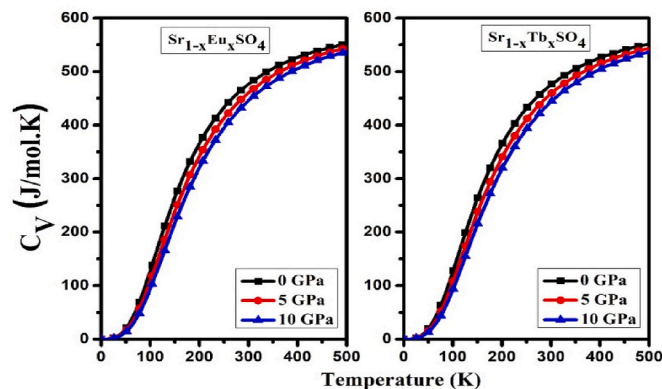

Fig. 13. Calculated thermal expansion coefficient at various pressures and temperatures for [SrSO$_4$]:Eu^{+2} and [SrSO$_4$]:Tb^{+2}.

Fig. 14. Calculated specific heat at constant volume at various pressures and temperatures for [SrSO$_4$]:Eu^{+2} and [SrSO$_4$]:Tb^{+2}.
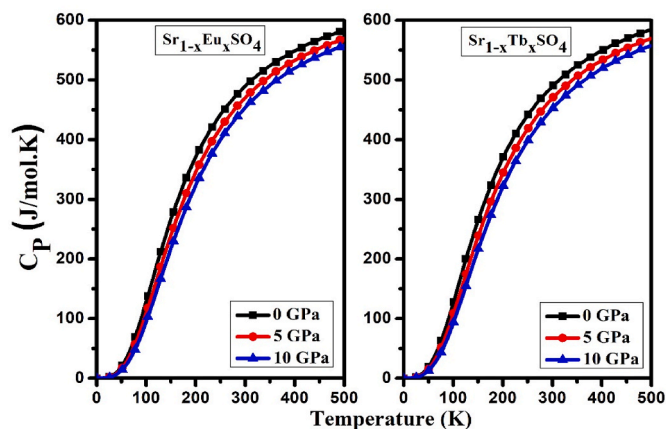
Fig. 15. Calculated specific heat at constant pressure at various pressures and temperatures for [SrSO$_4$]:Eu^{+2} and [SrSO$_4$]:Tb^{+2}.

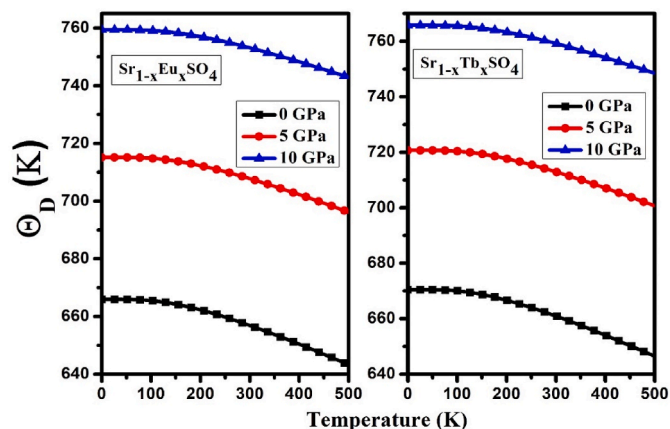**Fig. 16.** Calculated Debye temperature at various pressures and temperatures for [SrSO$_4$]:Eu^{+2} and [SrSO$_4$]:Tb^{+2}.
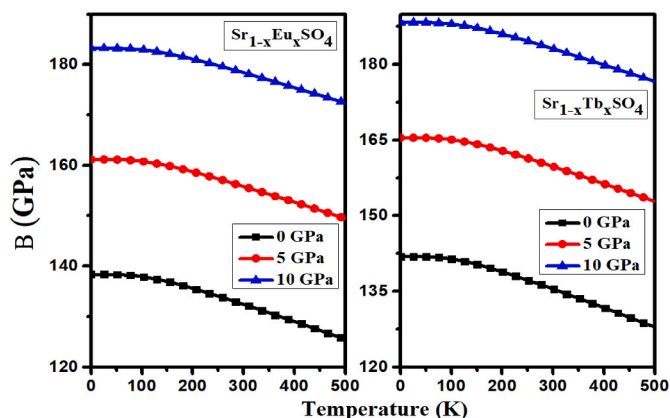

Fig. 17. Calculated Bulk Modulus at various pressures and temperatures for [SrSO$_4$]:Eu^{+2} and [SrSO$_4$]:Tb^{+2}.

3.4. Thermoelectric properties

Thermoelectric materials are utilized to produce electrical energy efficiently. Now a days, scientists are studying and working on the properties of such materials in order to develop applications for them e.g detector components, computer cooling, thermoelectric refrigeration etc. The thermoelectric properties are crucial and provide value able

information about studied materials at different temperatures and carrier concentrations. The thermoelectric properties of [SrSO$_4$]:Eu^{2+} and [SrSO$_4$]:Tb^{2+} have been calculated in the temperature interval 500 K $\leq$ T $\leq$ 800 K by using of semi-classical Boltzmann theory implemented in the Boltzmann simulation code. The materials have attained good thermoelectric efficiency when they have a high value of electrical conductivity and a low value of thermal conductivity. The Seebeck coefficient, which is formed as a result of temperature differences, is another important parameter that is given as $\frac{V}{\Delta T}$. The contribution of thermal energy is large at the hot end due to the adjustment of two different conductors. The higher value of the Seebeck coefficient provides a good figure of merit, which is a parameter conversion of wasted heat into useful purposes.

Thermal conductivity refers to the flow of heat caused by a temperature difference from a high to a low temperature. The flow of free electrons conducts heat in metals, while lattice vibrations carry heat in semi-conductors. For good TE materials, thermal conductivity plays a key role and is assumed to be low value in thermoelectric generator applications. The electronic thermal conductivity for Sr$_{1-x}$Eu$_x$SO$_4$ and Sr$_{1-x}$Tb$_x$SO$_4$ compounds is shown in Fig. 18. The results of thermal conductivity observed in our computations match with other so far reported compounds [39,47,55–58].

The thermal conductivity curve till 650 K shows no change and remains stood at zero. Beyond the temperature of 650 K, the thermal conductivity (κ) curve started with the lesser value for both the compounds and quickly reach at its higher value as noted in Table 1 at about 800 K. This follows a similar pattern to electrical conductivity (σ) as illustrated in Fig. 7. From the electrical and thermal conductivity curves, which have a similar profile, we have confirmed the Wiedemann-Franz law, according to which the contribution of electronic thermal conductivity is directly in proportional to the electrical conductivity [46,59, 60].

Another key parameter for computations of TE properties is electrical conductivity, which contains a large value for good performance. The heating effect is minimized by achieving a high value of electrical conductivity due to the joule heating effect. The calculated result of electrical conductivity for Sr$_{1-x}$Eu$_x$SO$_4$ and Sr$_{1-x}$Tb$_x$SO$_4$ is shown in Fig. 19 from 500 to 800 K. It can be analyzed from the mentioned figure, there is no change seen till 650 K for both investigated materials, but a very high value occurred at 800 K for Sr$_{1-x}$Tb$_x$SO$_4$. Both investigated materials show increasing trends in electrical conductivity, this is because they both get sufficient energy by raising the temperature. The electrical conductivity is tabulated in Table 1 for both the understudy compounds.

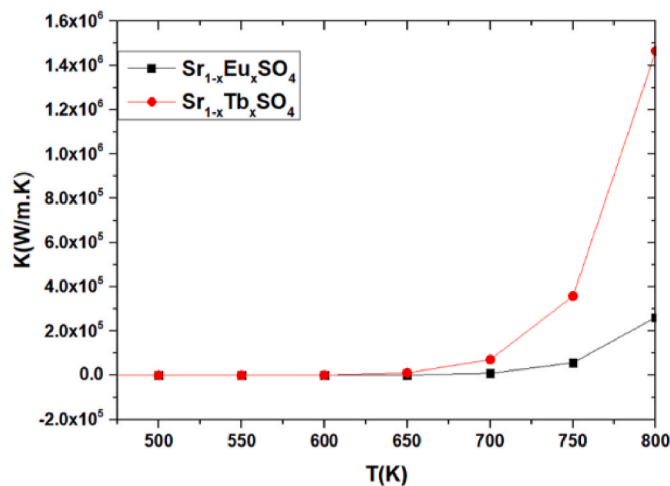The Seebeck coefficient is computed under the assumption of

Fig. 18. Calculated thermal conductivity at various temperatures for [SrSO$_4$]: Eu^{+2} and [SrSO$_4$]:Tb^{+2}.

Table 1
Calculated values of $Sr_{1-x}Eu_xSO_4$ and $Sr_{1-x}Tb_xSO_4$ compounds Thermoelectric Parameters.

Compounds	Seebeck coefficient (μV/K)	Thermal conductivities (W/m.K)	Electrical conductivities ($\Omega^{-1}cm^{-1}$)	Power factor (W/mK^2)	ZT
$Sr_{1-x}Eu_xSO_4$	3.07×10^{-3}	2.63×10^5	0.716×10^8	3.24×10^2	1.0014
$Sr_{1-x}Tb_xSO_4$	3.12×10^{-3}	1.46×10^6	4.64×10^8	1.83×10^3	1.0027

constant relaxation time without fitting parameters for $Sr_{1-x}Eu_xSO_4$ and $Sr_{1-x}Tb_xSO_4$ compounds, and plotted in Fig. 20. According to the figure, both materials achieve isotropic nature as seen in the electrical conductivity part (S remains at zero) until 500 K for $Sr_{1-x}Eu_xSO_4$ and 450 K for $Sr_{1-x}Tb_xSO_4$. The positive values of S exhibit that both compounds show P Type (the Hole carriers dominate the electronic transport) nature over the entire mentioned temperature range. Further beyond these mentioned temperatures, the curve increases sharply and reaches its peak values as noted in Table 1 for both the compounds. The highest values of S recorded for $Sr_{1-x}Eu_xSO_4$ and $Sr_{1-x}Tb_xSO_4$ compounds are 3.076×10^{-3} (μV/K) and 3.12×10^{-3} (μV/K), at a temperature of roughly 550 and 500 K, respectively.

Power factor depends upon relaxation time and hence it is related to electrical conductivity, written as PF/ τ. The power factor is used to check the efficiency of materials ($P.F = S^2\sigma$), the variations of PF by temperature are shown in Fig. 21 for $Sr_{1-x}Eu_xSO_4$ and $Sr_{1-x}Tb_xSO_4$ compounds. From the mentioned figure, there is no change seen in PF spectra till 650 K for both investigated materials. Further beyond this mentioned temperature, the curve increases sharply and reaches its peak values as noted in Table 1 for both the compounds. It is observed that $Sr_{1-x}Tb_xSO_4$ material exhibits a high value at 800 K as compared to $Sr_{1-x}Eu_xSO_4$. Moreover, as seen in Fig. 19, electrical conductivity (σ) reaches its maximum value with the same trend at the same temperature. It is observed that both materials are good at high temperatures instead of low temperatures region. So, by obtaining a high PF value, the $Sr_{1-x}Tb_xSO_4$ compound is good in waste heat management systems.

The efficiency of thermoelectric materials is investigated by (ZT) figure of merit. The material acquiring a high value could be more effective, which is possible at high electrical conductivity, Seebeck coefficient and lower values of thermal conductivity as indicated in Fig. 22 for $Sr_{1-x}Eu_xSO_4$ and $Sr_{1-x}Tb_xSO_4$ compounds. It is observed that $Sr_{1-x}Tb_xSO_4$ has a higher figure of merit compared to $Sr_{1-x}Eu_xSO_4$ as noted in Table 1 throughout the temperature range (500–800 K). The spectra for both understudy compounds begin at (ZT > 1) and increase/decrease with temperature, reaching a maximum (about 1.0027) value for $Sr_{1-x}Tb_xSO_4$ at 700 K and a minimum (about 0.988) value for $Sr_{1-x}Eu_xSO_4$ at

Fig. 20. Calculated Seebeck coefficient at various temperatures for [SrSO$_4$]: Eu^{+2} and [SrSO$_4$]:Tb^{+2}.
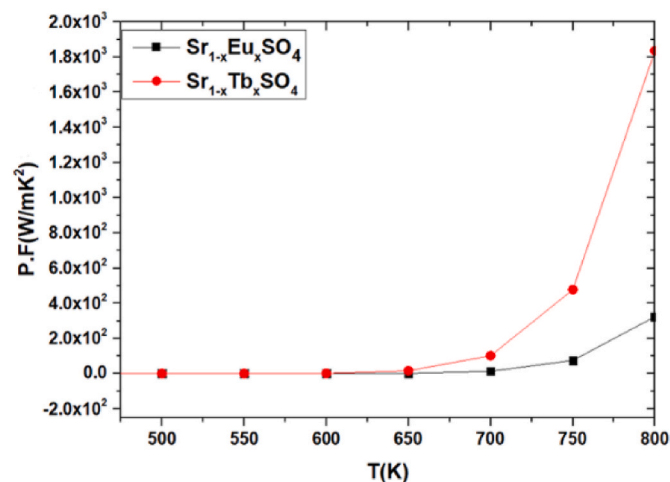
Fig. 21. Calculated Power Factor at various temperatures for [SrSO$_4$]:Eu^{+2} and [SrSO$_4$]:Tb^{+2}.

800 K. Furthermore, at 550 K, both compounds exhibited the same ZT value of 1.0014, but at around 800 K, $Sr_{1-x}Eu_xSO_4$ lags behind $Sr_{1-x}Tb_xSO_4$, as seen in the ZT plots.

4. Conclusions

The density functional theory (DFT) based WIEN2K simulation code is used in this study to calculate the ground state properties of [SrSO$_4$]: Eu^{2+} and [SrSO$_4$]:Tb^{2+} compounds with the help of FP-LAPW method. To determine the electrical and optical properties of $Sr_{1-x}A_xSO_4$ (A = Eu^{2+}, Tb^{2+}), the Generalized gradient approximation with the addition of the Hubbard parameter (GGA + U) was utilized. The obtained band structure results of $Sr_{1-x}Eu_xSO_4$ compound show semiconducting nature through both spin states, while the $Sr_{1-x}Tb_xSO_4$ compound depicts full-
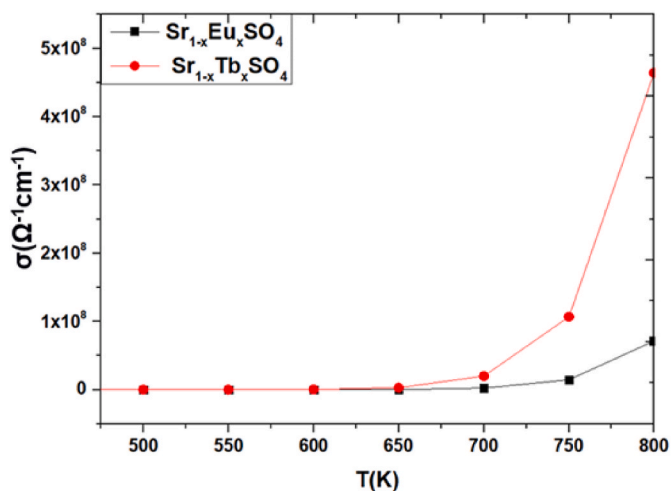

Fig. 19. Calculated Electrical conductivity at various temperatures for [SrSO$_4$]: Eu^{+2} and [SrSO$_4$]:Tb^{+2}.

Fig. 22. Calculated ZT at various temperatures for $[SrSO_4]:Eu^{+2}$ and $[SrSO_4]:Tb^{+2}$.

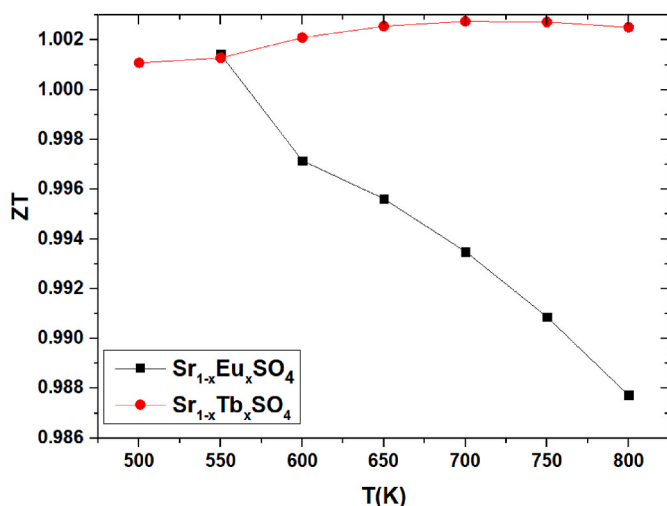metallic nature due to the crossing mechanisms of the conduction band minimum across the Fermi energy level. From demonstration of projected densities, it can be further characterized by the electrons transition from O[p] and Sr[p, d] orbitals in the valence band to S[s], O/S[p] and Eu/Tb/Sr[d] orbitals in the conduction band for $Sr_{1-x}Eu_xSO_4$ and $Sr_{1-x}Tb_xSO_4$, respectively. According to a theoretical assessment of optical properties, the compounds under investigation are promising possibilities for active optical devices working in the Ultra violet region. By obtaining these optical results in the energy range between 4 and 14eV, the studied compounds can be utilized as a shielding material due to high thermoelectric responses along with a promising blockage from solar heating in this region. The positive values of Seebeck coefficient exhibit that the material shows a P Type nature due to the dominancy of the hole carriers in electronic transport. The finding shows that $Sr_{1-x}Eu_xSO_4$ and $Sr_{1-x}Tb_xSO_4$ compounds are promising for future advanced optical and thermoelectric devices.

CRediT authorship contribution statement

Abdul Ahad Khan: Conceptualization, Data curation, Investigation, Methodology, Writing – original draft, Writing – review & editing. **Zeesham Abbas:** Conceptualization, Formal analysis, Investigation, Methodology, Writing – original draft, Writing – review & editing. **Zeshan Zada:** Conceptualization, Data curation, Investigation, Methodology, Project administration, Resources, Software, Writing – original draft, Writing – review & editing. **Rifaqat Zada:** Formal analysis, Validation, Visualization, Writing – original draft, Writing – review & editing. **Fazal Ur Rehman M:** Formal analysis, Validation, Visualization, Writing – review & editing. **Muhammad Irfan:** Formal analysis, Validation, Visualization, Writing – review & editing. **G. Murtaza:** Formal analysis, Project administration, Resources, Software, Supervision, Validation, Visualization, Writing – review & editing. **Muhammad Ismail:** Formal analysis, Validation, Visualization, Writing – review & editing. **Qaisar Khan:** Formal analysis, Validation, Visualization, Writing – review & editing. **Muhammad Ismail:** Formal analysis, Validation, Visualization, Writing – review & editing. **Muhammad Ishaq:** Formal analysis, Validation, Visualization, Writing – review & editing.**Sajjad Hussain:** Formal analysis, Validation, Visualization, Writing – review & editing. **Ali H. Reshak:** Formal analysis, Project administration, Resources, Validation, Visualization, Writing – original draft, Writing – review & editing.

Declaration of competing interest

The authors declare that they have no known competing financial interests or personal relationships that could have appeared to influence the work reported in this paper.

Data availability

Data will be made available on request.

References

[1] M. Mehrabi, M. Zahedifar, S. Hasanloo, H. Nikmanesh, R. Gheisari, Y. Li, Preparation and characterization of Li2B4O7 nanoparticles co-doped with Mg and Cu for thermoluminescence dosimetry of gamma-rays, Radiat. Phys. Chem. 194 (2022), 110057.

[2] M.T. Lee, D.J. Hwang, R. Greif, C.P. Grigoropoulos, Nanocatalyst fabrication and the production of hydrogen by using photon energy, Int. J. Hydrogen Energy 34 (4) (2009) 1835–1843.

[3] Y. Zhu, X. Wu, Heterostructured materials, Prog. Mater. Sci. (2022), 101019.

[4] M. Zahedifar, M. Mehrabi, Thermoluminescence and photoluminescence of cerium doped CaSO4 nanosheets, Nucl. Instrum. Methods Phys. Res. Sect. B Beam Interact. Mater. Atoms 268 (23) (2010) 3517–3522.

[5] E. De la Rosa, R.A. Rodríguez, R. Melendrez, P. Salas, L.A. Diaz-Torres, M. Barboza-Flores, Thermoluminescence properties of undoped and Tb3+ and Ce3+ doped YAG nanophosphor under UV-, X-and β-ray irradiation, Nucl. Instrum. Methods Phys. Res. Sect. B Beam Interact. Mater. Atoms 255 (2) (2007) 357–364.

[6] A.R. Kadam, Y.R. Parauha, M. Michalska-Domanska, N.S. Dhoble, S.J. Dhoble, Nanophosphors for radiation dosimetry, in: Radiation Dosimetry Phosphors, Woodhead Publishing, 2022, pp. 251–277.

[7] K.B. Jamkhaneh, K.R.E. Saraee, Thermoluminescence characterization of nanocrystalline powder of SrSO4: Sm exposed to gamma radiation for dosimetric applications, Appl. Radiat. Isot. 160 (2020), 109128.

[8] S. Jayasudha, K. Madhukumar, C.M.K. Nair, R.G. Nair, V.M. Anandakumar, T.S. Elias, Structural characterization, thermoluminescence studies and kinetic parameters of SrSO4: Eu nanophosphors under X-ray and gamma excitations, Spectrochim. Acta Mol. Biomol. Spectrosc. 155 (2016) 21–27.

[9] E.G. Yukihara, S.W. McKeever, C.E. Andersen, A.J. Bos, I.K. Bailiff, E.M. Yoshimura, J.B. Christensen, Luminescence dosimetry, Nat. Rev. Methods Prim. 2 (1) (2022) 1–21.

[10] M.T. Jose, U. Madhusoodanan, A.R. Lakshmanan, Influence of (group IIB) codopants on the thermostimulated luminescence sensitivity of CaSO4: Dy/Tm, J. Phys. Appl. Phys. 34 (5) (2001) 717.

[11] Z. Chunxiang, C. Lixin, T. Qiang, L. Daling, Q. Zhiren, Emission spectra of MgSO4: Dy, MgSO4: Tm and MgSO4: Dy, Mn phosphors, Radiat. Meas. 32 (2) (2000) 123–128.

[12] V. Kortov, Materials for thermoluminescent dosimetry: current status and future trends, Radiat. Meas. 42 (4–5) (2007) 576–581.

[13] M. Kerikmäe, M. Danilkin, I. Jaek, M. Must, A. Ots, L. Pung, T. Tõnutare, OSL and TSL interrelations in SrSO4: Eu, Radiat. Meas. 45 (3–6) (2010) 559–561.

[14] C.X. Zhang, Q. Tang, D.L. Luo, Z.R. Qiu, P.L. Leung, M.J. Stokes, Investigation of the TL mechanism and defect structure in MgSO4 doped with Eu and Mn, P impurities, Radiat. Meas. 35 (2) (2002) 161–166.

[15] Q. Tang, C.X. Zhang, D.L. Luo, P.L. Leung, Z.Y. Xiong, TL and OSL of SrSO4 phosphors doped with Eu, Radiat. Protect. Dosim. 119 (1–4) (2006) 238–243.

[16] R. Fujimaki, Y. Oaki, H. Imai, A nonclassical pathway to biomimetic strained SrSO 4 crystals, CrystEngComm 24 (2022) 4356–4360.

[17] O. Öztürk, Ş.N. Karaburç, M. Saydan, Ü.S. Keskin, High rate X-ray radiation shielding ability of cement-based composites incorporating strontium sulfate (SrSO4) minerals, Kerntechnik 87 (1) (2022) 115–124.

[18] B.F. Esteves, E. Spielman-Sun, Q. Li, A.D. Jew, J.R. Bargar, J.L. Druhan, Geochemical modeling of celestite (SrSO4) precipitation and reactive transport in shales, Environ. Sci. Technol. 56 (7) (2022) 4336–4344.

[19] A. Saim, F. Belkharroubi, F.Z. Boufadi, I. Ameri, L.F. Blaha, A. Tebboune, A. El-Rehim, Investigation of the structural, elastic, electronic, and optical properties of half-heusler CaMgZ (Z= C, Si, Ge, Sn, Pb) compounds, J. Electron. Mater. 51 (7) (2022) 4014–4028.

[20] L. Samia, F. Belkharroubi, A. Ibrahim, B.F. Lamia, A. Saim, A. Maizia, Y. Al-Douri, Investigation of structural, elastic, electronic, and magnetic proprieties for X2LuSb (X= Mn and Ir) full-Heusler alloys, Emergent Mater. 5 (2) (2022) 537–551.

[21] B. Asma, F. Belkharroubi, A. Ibrahim, B. Lamia, A. Mohammed, W. Belkilali, Y. Al-Douri, Structural, mechanical, magnetic, electronic, and thermal investigations of Ag2YB (Y= Nd, Sm, Gd) full-Heusler alloys, Emergent Mater. 4 (6) (2021) 1769–1783.

[22] K. Radja, B.L. Farah, A. Ibrahim, D. Lamia, I. Fatima, B. Nabil, A.F. Abd El-Rehim, Investigation of structural, magneto-electronic, elastic, mechanical and thermoelectric properties of novel lead-free halide double perovskite Cs2AgFeCl6: first-principles calculations, J. Phys. Chem. Solid. (2022) 110795.

[23] F. Kadi, M. Zemouli, H. Boutaleb, Z. Akil, K. Amara, M. Elkeurti, Structural, elastic, electronic, optic and thermodynamic properties of Li2BaSnX4 (X= S and Se) alloys: a first-principle study, Comput. Condens. Matter 32 (2022), e00718.

[24] I. Zerifi, A. Assali, A. Boukortt, L. Chaabane, First-principles investigation on narrow bandgap InSb1− xBix dilute bismide alloys for highly efficient long-wavelength infrared optoelectronics, Infrared Phys. Technol. 125 (2022), 104319.

[25] W. Belkilali, F. Belkharroubi, M. Ameri, N. Ramdani, F. Boudahri, F. Khelfaoui, Y. Al-Douri, Theoretical investigations of structural, mechanical, electronic and optical properties of NaScSi alloy, Emergent Mater. 4 (5) (2021) 1465–1477.

[26] M.K. Zoubir, B. Fadila, B. Keltoum, A. Ibrahim, B.L. Farah, Y. Al-Douri, A. Mohammed, Structural, electronic and thermodynamic investigation of Ag2GdSi, Ag2GdSn and Ag2Gd Pb Heusler alloys: first-principles calculations, Mater. Test. 63 (6) (2021) 537–542.

[27] A. Khireddine, A. Bouhemadou, S. Alnujaim, N. Guechi, S. Bin-Omran, Y. Al-Douri, A.K. Kushwaha, First-principles predictions of the structural, electronic, optical and elastic properties of the zintl-phases AE3GaAs3 (AE= Sr, Ba), Solid State Sci. 114 (2021), 106563.

[28] I. Rahim, S. Azam, B. Gul, A.A. Khan, N. Yousaf, Z. Zada, H.H. Hegazy, Advances in tuning band gap of graphene by potential doping using DFT: a review, Digest J. Nanomater. Biostructures 16 (3) (2021).

[29] K. Boudiaf, A. Bouhemadou, Y. Al-Douri, R. Khenata, S. Bin-Omran, N. Guechi, Electronic and thermoelectric properties of the layered BaFAgCh (Ch= S, Se and Te): first-principles study, J. Alloys Compd. 759 (2018) 32–43.

[30] N. Guechi, A. Bouhemadou, Y. Medkour, Y. Al-Douri, R. Khenata, S. Bin-Omran, Electronic and thermoelectric properties of the layered Zintl phase CaIn2P2: first-principles calculations, Phil. Mag. 100 (23) (2020) 3023–3039.

[31] S. Ostermann, K. Plankensteiner, R. Prodan, T. Fahringer, Groudsim: an event-based simulation framework for computational grids and clouds, in: European Conference on Parallel Processing, Springer, Berlin, Heidelberg, 2010, August, pp. 305–313.

[32] Z. Abbas, S. Azam, A.I. Bashir, A. Marriam, M. Waqas, T. Alshahrani, B.U. Haq, A systematic study on optoelectronic properties of Mn4+-activated Zr-based hexafluoride red phosphors X2ZrF6 (X= K, Na, Cs): first-principles investigation and prospects for warm-white LEDs applications, Phys. Scripta 96 (1) (2020), 015801.

[33] Z. Zada, A.A. Khan, A.H. Reshak, M. Ismail, S. Zada, G. Murtaza, J. Bila, Cationic variation for LnAl2Si2 (Ln= Y, Sm, Tb, Dy, Yb) compounds by density functional theory, J. Mol. Struct. 1252 (2022), 132136.

[34] A.A. Khan, Z. Zada, A.H. Reshak, J. Akbar, M. Saqib, M.A. Naeem, M.M. Ramli, Effects of anion-ligands replacement on the structural, electronic and magnetic properties of ThCo2X2 (X= Si, Ge), Chin. J. Phys. 77 (2022) 956–964.

[35] Z. Zada, A.A. Khan, R. Zada, A.H. Reshak, G. Murtaza, M. Saqib, J. Bila, First-principles calculations to investigate variation of cationic-ligand LmAl2Ge2 (Lm= Ca, Y, La and Ce), Indian J. Phys. (2022) 1–9.

[36] Z. Zada, A. Laref, G. Murtaza, A. Zeb, A. Yar, First-principles calculations of electronic and magnetic properties of XMn2Y2 (X= Ca, Sr; Y= Sb, Bi) compounds, Int. J. Mod. Phys. B 33 (18) (2019), 1950199.

[37] Z. Zada, H. Ullah, R. Bibi, S. Zada, A. Mahmood, Electronic band profiles and magneto-electronic properties of ternary XCu2P2 (X= Ca, Sr) compounds: insight from ab initio calculations, Z. Naturforsch. 75 (6) (2020) 543–549.

[38] A. Otero-de-la-Roza, V. Luaña, Equations of state and thermodynamics of solids using empirical corrections in the quasiharmonic approximation, Phys. Rev. B 84 (18) (2011), 184103.

[39] R. Bibi, Z. Zada, A.A. Khan, S. Azam, M. Irfan, B.U. Haq, S.A. Khan, First-principles calculations of structural, electronic, magnetic, thermoelectric, and thermodynamic properties of BaMn2P2 in the Anti and ferromagnetic phase, J. Solid State Chem. 302 (2021), 122388.

[40] M.A. Blanco, A.M. Pendás, E. Francisco, J.M. Recio, R. Franco, Thermodynamical properties of solids from microscopic theory: applications to MgF2 and Al2O3, J. Mol. Struct.: THEOCHEM 368 (1996) 245–255.

[41] G.K. Madsen, D.J. Singh, BoltzTraP. A code for calculating band-structure dependent quantities, Comput. Phys. Commun. 175 (1) (2006) 67–71.

[42] G. Murtaza, A.A. Khan, M. Yaseen, A. Laref, N. Ullah, I. ur Rahman, The effect of replacing pnictogen elements on the physical properties SrMg2 (, P, As, Sb, Bi) Zintl compounds, Chin. Phys. B 27 (4) (2018), 047102.

[43] D.R. Penn, Wave-number-dependent dielectric function of semiconductors, Phys. Rev. 128 (5) (1962) 2093.

[44] A.A. Khan, W. Khan, A. Khan, A. Laref, A. Zeb, G. Murtaza, Investigation of the structural, electrical, optical and magnetic properties of XMg4Mn6O15 (X= K, Rb, and Cs) compounds, Mater. Res. Express 6 (6) (2019), 066102.

[45] Z. Khan, G. Murtaza, A.A. Khan, A. Laref, N.A. Kattan, M. Haneef, Different physical properties of bi-alkali pnictogen compounds using density functional theory, Int. J. Energy Res. 45 (5) (2021) 7703–7718.

[46] A.A. Khan, M. Yaseen, A. Laref, G. Murtaza, Impact of anion replacement on the optoelectronic and thermoelectric properties of CaMg2X2, X=(N, P, As, Sb, Bi) compounds, Phys. B Condens. Matter 541 (2018) 24–31.

[47] A.A. Khan, A.H. Reshak, Z. Noor, G. Murtaza, M.M. Al-Anazy, H. Althib, J. Bila, First-principles calculations of structural, electronic, optical, and thermoelectric properties of ternary d-metal sulfides Sc2CdS4 and Y2CdS4 compounds, Int. J. Energy Res. (2021).

[48] C.Z. Wang, C.T. Chan, K.M. Ho, Tight-binding molecular-dynamics study of phonon anharmonic effects in silicon and diamond, Phys. Rev. B 42 (17) (1990), 11276.

[49] L.J. Porter, J.F. Justo, S. Yip, The importance of Grüneisen parameters in developing interatomic potentials, J. Appl. Phys. 82 (11) (1997) 5378–5381.

[50] H.B. Ozisik, K. Colakoglu, G. Surucu, H. Ozisik, Structural and lattice dynamical properties of Zintl NaIn and NaTl compounds, Comput. Mater. Sci. 50 (3) (2011) 1070–1076.

[51] Z. Zada, H. Ullah, R. Zada, A.A. Khan, A. Mahmood, S.M. Ramay, Electronic band profiles, magnetic stability, antiferromagnetic spins ordering and thermodynamics properties of novel antiferromagnet CaCr 2 Sb 2, Eur. Phys. J. Plus 136 (4) (2021) 1–13.

[52] M. Siddique, A. Iqbal, A.U. Rahman, S. Azam, Z. Zada, N. Talat, Mechanical and thermodynamic stability, structural, electronics and magnetic properties of new ternary thorium-phosphide silicides ThSixP1-x: first-principles investigation and prospects for clean nuclear energy applications, Nucl. Eng. Technol. 53 (2) (2021) 592–602.

[53] A.A. Khan, A.H. Reshak, Z. Zada, M. Saqib, Z. Abbas, M. Ismail, A. Laref, Thermoelectric, structural, electronic, magnetic, and thermodynamic properties of CaZn2Ge2 compound, Eur. Phys. J. Plus 137 (3) (2022) 1–12.

[54] Z. Zada, R. Zada, A.A. Khan, M. Saqib, M.F.U. Rehman, M. Ismail, M. Faizan, Investigation of electronic structure, magnetic stability, spin coupling, and thermodynamic properties of novel antiferromagnets XMn2Y2 (X= Ca, Sr; Y= P, As), J. Mol. Struct. 1268 (2022), 133698.

[55] A.A. Khan, A.U. Rehman, A. Laref, M. Yousaf, G. Murtaza, Structural, optoelectronic and thermoelectric properties of ternary CaBe2X2 (X= N, P, As, Sb, Bi) compounds, Z. Naturforsch. 73 (10) (2018) 965–973.

[56] G. Murtaza, A.A. Khan, M.M. Al-Anazy, A. Laref, Q. Mahmood, Z. Zada, M. Aman, Anionic variations for BaMg 2 X 2 (X= N to Bi) compounds by density functional theory, Eur. Phys. J. Plus 136 (2) (2021) 1–16.

[57] Z. Zada, H. Ullah, R. Zada, S. Zada, A. Laref, S. Azam, M. Irfan, Structure stability, half metallic ferromagnetism, magneto-electronic and thermoelectric properties of new zintl XCr2Bi2 (X= Ca, Sr) compounds for spintronic and renewable energy applications, Phys. B Condens. Matter 607 (2021), 412866.

[58] A.A. Khan, M. Saqib, Z. Zada, F. Chahed, M. Ismail, M. Ishaq, M. Faizan, Electronic structure, magnetic, and thermoelectric properties of BaMn2As2 compound: a first-principles study, Phys. Scripta 97 (6) (2022), 065810.

[59] A.A. Khan, R. Hasil, A. Laref, N. Ullah, M. Sajjad, A. Zeb, G. Murtaza, DFT prediction of the structural, electronic, thermoelectric and optical properties of ternary pnictides MgBe2X2 (X= N, P, As, Sb, Bi): a novel analysis of beryllium with 2A-and 5B-elements of the structure type CaAl2Si2, Solid State Commun. 300 (2019), 113667.

[60] M.A. Boudjeltia, Z. Aziz, S. Terkhi, M.A. Bennani, S.A. Khandy, B. Bouadjemi, S. Bentata, Theoretical investigation of ternary semiconductors half-Heusler RhTaZ (Z= Si, Ge and Sn) for thermoelectric applications, Mod. Phys. Lett. B 35 (23) (2021), 2150400.